Chemical Science

Accepted Manuscript

This article can be cited before page numbers have been issued, to do this please use: T. Nishiguchi, K. Kageyama, T. Kurihara, N. Shimanaka, S. Tokuda, S. Tsuda, N. Ma and S. Horike, *Chem. Sci.*, 2026, DOI: 10.1039/D5SC06222E.

ROYAL SOCIETY OF CHEMISTRY

rsc.li/chemical-science

View Article Online
DOI: 10.1039/D5SC06222E

ARTICLE

Soft crystalline properties of 2D frameworks constructed from lithium ion and dinitriles

Received 00th January 20xx,
Accepted 00th January 20xx

DOI: 10.1039/x0xx00000x

Taichi Nishiguchi,‡[a] Kotoha Kageyama,‡[b] Takuya Kurihara,[c] Nanae Shimanaka,[d] Shun Tokuda,[bd] Shuto Tsuda,[a] Nattapol Ma[b] and Satoshi Horike*[ade]

We constructed two-dimensional (2D) molecular frameworks composed of lithium ion (Li^+) and dinitrile aliphatic ligands to explore their mechanical and thermal properties. Calorimetry, X-ray diffraction, density functional theory calculations, alternating current impedance, and solid-state nuclear magnetic resonance evidenced behaviours and properties originating from the weakly-linked 2D system. We found low melting temperatures (< 100 °C), high mechanical deformability, large positive and negative thermal expansion, and metal ion diffusion. These were uniquely observed in the integration of $Li^+$and dinitriles into the extended molecular structures.

Introduction

Coordination polymers (CPs) and metal–organic frameworks (MOFs) are molecular frameworks featuring well-defined, periodic structures. Conventional design and synthesis of CP/MOFs have focused on the robustness and stability of the frameworks based on stronger coordination bonds by applying high-valent transition metal ions such as oxophilic Zr^{4+} and Cr^{3+}, and rigid ligands.[1,2] On the other hand, frameworks based on weaker metal–ligand interactions have been relatively unexplored, despite their potential to exhibit distinct dynamic and thermomechanical behaviours.

In recent studies, synthetic approaches to incorporate the weak metal–ligand interaction have adopted to create CP/MOF crystals with phase change, including melting behaviours.[3–7] Controlling the bond strength (enthalpic factor) and the mobility of molecular components (entropic factor) reduces the melting temperature (T_m) to a value lower than the decomposition temperature to give a stable liquid state.[8,9] In other words, CP/MOFs constructed from metal ions and bridging ligands with weak interactions would represent not only the melting phenomena but also explore unique physical (especially, thermal) properties in the crystalline state; however, many of them have been overlooked.

Here, we report molecular frameworks constructed from lithium ions (Li^+) and dinitriles. We selected Li^+ as nodes and dinitrile aliphatic linkers to construct crystalline frameworks, utilising their non-directional bonding and the inherent flexibility of the linker molecules.[10–13] Solvent-free melt-cooling reaction was employed instead of self-assembling process in solutions to incorporate these components in the single crystalline phases. The crystalline products are two-dimensional (2D) structures, and exhibit low T_m ranging from 59 to 90 °C, below those typically reported for CP/MOFs. They exhibited Young's moduli below 18 GPa, and one compound showed large positive and negative thermal expansion, with the absolute value of the coefficient exceeding 100 × 10^{-6} K^{-1}. The weak interactions between the metal and ligands facilitate dissociation of the coordination interactions, resulting in the diffusion of the metal ions in the crystalline phase.

Results and discussion

Crystal structures

Four Li-based frameworks, $Li(FSI)(SN)_2$ (**1**), $Li(FSI)(GN)_2$ (**2**), $Li(FSI)(SN)(GN)$ (**3**), and $Li(TFSI)(SN)_{1.5}$ (**4**) (FSI^- = bis(fluorosulfonyl)imide, $TFSI^-$ = bis(trifluoromethanesulfonyl)imide, SN = succinonitrile, GN = glutaronitrile) were synthesised (see ESI for the detailed synthetic methods).[10,14–16] Solvent-free melt-cooling reaction was performed under an Ar atmosphere to effectively trap the metastable, weak interactions in the crystalline states. This reaction is necessary because no crystals were formed using conventional solvothermal reactions with ethanol, acetonitrile, or tetrahydrofuran. In Fig. 1 and S1, we reveal the structures

[a] Department of Chemistry, Graduate School of Science, Kyoto University, Kitashirakawa-Oiwakecho, Sakyo-ku, Kyoto 606-8502, Japan
[b] Department of Synthetic Chemistry and Biological Chemistry, Graduate School of Engineering, Kyoto University, Katsura, Nishikyo-ku, Kyoto 615-8510, Japan
[c] Division of Material Chemistry, Graduate School of Natural Science and Technology, Kanazawa University, Kakuma-Machi, Kanazawa, Ishikawa 920-1192, Japan
[d] Institute for Integrated Cell-Material Sciences, Institute for Advanced Study, Kyoto University, Yoshida-Honmachi, Sakyo-ku, Kyoto 606-8501, Japan
[e] Department of Materials Science and Engineering, School of Molecular Science and Engineering, Vidyasirimedhi Institute of Science and Technology, Rayong, 21210, Thailand

†Supplementary Information available: The details of experiments, crystallographic data, computational analyses, thermogravimetric analysis, differential scanning calorimetry, variable-temperature powder X-ray diffraction and fitting, impedance and ion conductivity measurements, and solid-state nuclear magnetic resonance (PDF). See DOI: 10.1039/x0xx00000x
‡ These authors contributed equally.

through single crystal X-ray diffraction (SC-XRD) analyses of **2**, **3**, and **4**, along with the previously reported structure of **1**. All obtained crystals consist of tetrahedral Li^+ and dinitrile linkers. **2**, **3**, and **4** feature 2D sheet structures. Compounds **2** and **3** consist of frameworks with tetracoordinated Li^+ and SN/GN linkers, containing FSI within them. In contrast, **4** has two inequivalent Li^+ sites; one site is coordinated with four SN, while the other has two SN and two $TFSI^-$. The $TFSI^-$ cap the sheets to form a 2D extended structure. The 2-nm sheets exhibit a **sql** topology, as determined by TOPOS Pro,[19] with a two-fold inclined interpenetration. Mixtures of $Li(BF_4)$ and SN, and $Li(PF_6)$ and SN at the molar ratio of 1/2 formed solids with unclear melting behaviours, suggesting the formation of impurity phases. These indicate the importance of FSI^- and $TFSI^-$ for the formation of pure single phases.

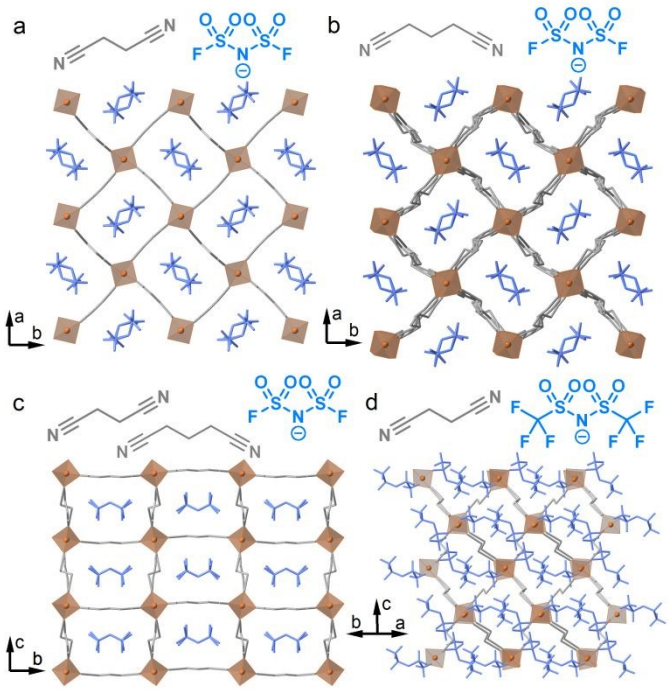

Fig. 1 Schematic representations of dinitriles and anions, and crystal structure of (a) $Li(FSI)(SN)_2$ (**1**) at −100 °C, (b) $Li(FSI)(GN)_2$ (**2**) at 0 °C, (c) Li(FSI)(SN)(GN) (**3**) at 0 °C, and (d) $Li(TFSI)(SN)_{1.5}$ (**4**) at −175 °C. SN/GN: grey, Li^+: orange, $FSI^-/TFSI^-$: blue. H atoms are omitted for clarity.

Thermal behaviours

Thermogravimetric analysis (TGA) determined the decomposition temperatures of **1–4** to be 109, 140, 139, and 139 °C (Fig. S2), forming a stable liquid state over a temperature window of 50 °C. In Fig. 2, differential scanning calorimetry (DSC) revealed melting peaks for **1–4** at 63, 90, 90, and 59 °C (Fig. 2a–d). T_m of **1** aligns with the report, suggesting a high phase purity.[10] Variable-temperature (VT) powder X-ray diffraction (PXRD) of powder samples, matching those simulated from SC-XRD structures, confirmed the complete transformation during melting (Fig. S3). We synthesised $Li(TFSI)(bpe)_2$ (bpe = 1,2-bis(4-pyridyl)ethane) to elucidate the role of the ligand in reducing T_m (Fig. S4, Table S1). It showed T_m of 219 °C in DSC, without significant weight loss in TGA (Fig. S5), a temperature comparable to reported $TFSI^-$- and pyridine-based melting CPs and analogues (168–245 °C).[10] This indicates the origin of the low T_m of **1–4** from the weak interaction between Li^+ and nitrile groups. In the DSC of **4**, a glass transition was observed at −48 °C (T_g) in the second heating process. This indicates the low diffusivity of the components due to the bulky $TFSI^-$ and a high Li^+/linker ratio, suppressing the crystallisation to form a glassy state.[25] We performed DSC at different ramping rates (Fig. S6). While 3 K min^{-1} or higher observed no crystallisation, the heating process at 2 K min^{-1} found crystallisation. This indicates that ramping rates above 2 K min^{-1} are required for the formation of a stable glassy/liquid phase of **4**.

To gain an understanding of low-melting behaviours, we studied the thermodynamic parameters. The melting enthalpy (ΔH_{fus}) and melting entropy (ΔS_{fus}) for **1**, **2**, **3**, and **4** are presented in Table 1. The lower ΔH_{fus} for **2** compared to **1** results from the increased cation–anion distances, which reduce the electrostatic stability of **2**.[8,26] According to the equation $T_m = \Delta H_{fus}/\Delta S_{fus}$, a higher ΔH_{fus} corresponds to a higher T_m. However, **2** exhibits a higher T_m than **1** despite its lower ΔH_{fus}. This can be attributed to the significantly lower ΔS_{fus} of **2**, highlighting the important role of entropy, which has been discussed in relation to ionic liquids CPs.[23,27] Among the low-melting MOFs, entropy also plays a significant role in their melting behaviours. The lower ΔS_{fus} of **2** despite the longer alkyl chain indicates the higher degree of freedom, or more 'liquid-like' dynamics of GN in **2**. The high ΔH_{fus} and ΔS_{fus} of **3** originate from the more densely packed structure, supported by the density (Table S1). The lower ΔH_{fus} and ΔS_{fus} of **4** are explained by the lower symmetry of the crystal and fewer aliphatic components in the composition.

In addition to the melting, small sharp peaks were observed in DSC of **1** and **2** at −69 and −12 °C (T_{ss}). The SST entropy (ΔS_{ss}) of **1** and **2** were 18.5 and 5.0 J K^{-1} mol^{-1}. They are equal to 2.2 *R* and 0.6 *R*, where *R* is the universal gas constant. These indicate the increase in number of states (*W*) by 9.3 and 1.8 times as derived from Boltzmann's equation; $S = R \ln(W)$.[28] The *W* of 1.8 for **2** is almost equal to 2, and this is consistent with the disordering of GN into two possible conformations at a higher temperature than T_{ss}. The *W* of 9.3 for **1** suggests the disordering of both SN and FSI^- in the SST.

View Article Online
DOI: 10.1039/D5SC06223F

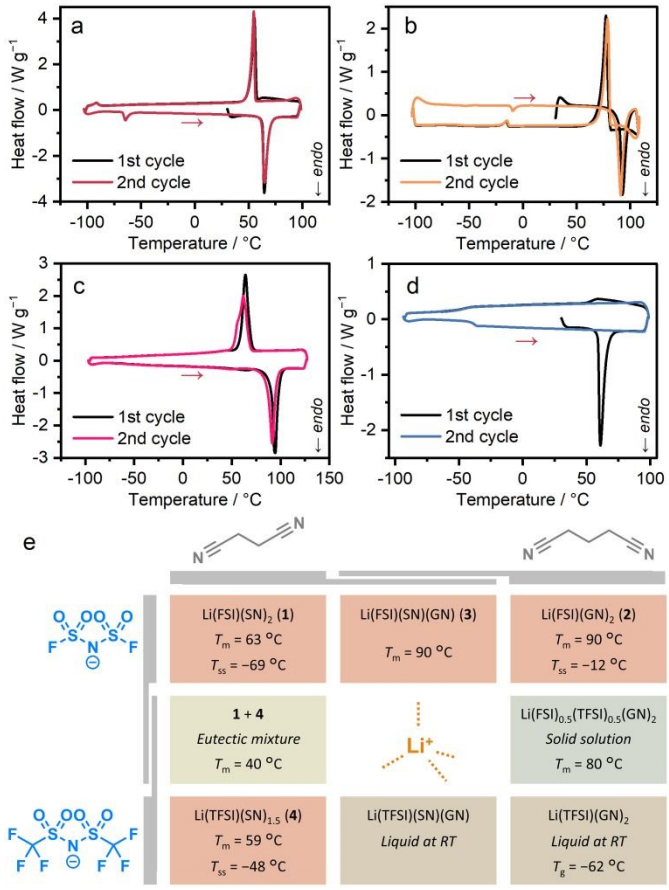

Fig. 2 DSC profiles of (a) **1**, (b) **2**, (c) **3**, and (d) **4**. Red arrows indicate heating processes. (e) Summary of thermal and phase behaviours.

Phase behaviours of mixtures and analogues

We investigated the mixture of the crystals and analogues to further understand the phase behaviours of the systems (Fig. 2e). We applied physical mixing for **1** and **2** with equimolar amounts. PXRD pattern after five-minute hand grinding in a mortar matched with that of **3** without diffractions of **1** or **2** (Fig. S7). The pattern was fitted with the space group of *Pbcm*, supporting the formation of **3** (Fig. S8, Table S2). This indicates the formation of **3**, suggesting high diffusivity of the components and formability of the crystalline state of **3**.

For the mixture of **1** and **4**, we studied $\mathbf{1}_x\mathbf{4}_{1-x}$ (x = 0.25, 0.5, 0.75), prepared by melt-cooling processes of the mixtures with the molar ratio of $x/(1-x)$ on the Li^+ basis. PXRD patterns after the melt-cooling process confirmed the co-presence of **1** and **4** crystal phases in all the mixtures without forming any new phases (Fig. S9). While $\mathbf{1}_{0.25}\mathbf{4}_{0.75}$ and $\mathbf{1}_{0.75}\mathbf{4}_{0.25}$ showed two melting peaks in DSC, $\mathbf{1}_{0.5}\mathbf{4}_{0.5}$ exhibited a single melting peak at 40 °C (Fig. S10). These indicate the formation of an eutectic mixture with T_m of 40 °C.[29,30] The ΔH_{fus} and ΔS_{fus} were analysed to elucidate the thermodynamic origin of the reduction of T_m (Table 1). ΔH_{fus} of 30 kJ mol^{-1} is comparable to the average of **1** and **4**, suggesting the absence of enthalpic stabilisation by mixing the crystals. ΔS_{fus} was calculated as $\Delta H_{fus}/T_m$ = 97 J K^{-1} mol^{-1}. This value is larger than the average of **1** and **4** ([101 + 80] / 2 = 91) by 6 J K^{-1} mol^{-1}, indicating the entropic contributions to the reduction of the T_m. The value of 6 J K^{-1} mol^{-1} is close to R ln(2), and this is interpreted as the term of mixing entropy (ΔS_{mix}) in the liquid state, which is given by the equation of for ideal solutions as $\Delta S_{mix} = -R\,[x\ln(x) + (1-x)\ln(1-x)]$. These highlight the pure and significant effect of the mixing entropy on the minimisation of the T_m of the mixture.

The mixture of Li(FSI), Li(TFSI), and GN at the molar ratio of 1:1:4 formed a colourless crystalline powder. DSC of the product observed a sharp melting peak at 80 °C (Fig. S11), suggesting the formation of a pure crystalline phase. PXRD pattern showed peaks at the comparable positions as those of **2** (Fig. S12), proving the formation of a solid solution state with randomised anion positions with the formula of $Li(FSI)_{0.5}(TFSI)_{0.5}(GN)_2$. We performed fitting of the PXRD pattern at 30 °C (Fig. S13). The extracted lattice constants are 0.1% larger than those of **2** (Table S3, S5), suggesting the expansion of the cell by including $TFSI^-$ inside the frameworks.

We also attempted the synthesis of Li(TFSI)–GN and Li(TFSI)–SN–GN frameworks with the corresponding formula of $Li(TFSI)(GN)_2$ and Li(TFSI)(SN)(GN). Each mixture of the precursors gave liquid states that remained uncrystallised over three years, forming a stable liquid state at room temperature. The DSC of $Li(TFSI)(GN)_2$ observed a glass transition at −62 °C (Fig. S14), a temperature lower than the T_g of **4** by 14 °C, suggesting a possible T_m of 38 °C, assuming the T_g/T_m ratio based on that of **4** (0.68, for the absolute temperatures). This suggests the T_m close to RT, preventing the crystal formation to give the RT liquid phase.

Table 1 Thermodynamic parameters of **1**–**4** and $\mathbf{1}_{0.5}\mathbf{4}_{0.5}$.

Sample	T_m / °C	ΔH_{fus} / kJ mol^{-1}	ΔS_{fus} / J K^{-1} mol^{-1}	T_{ss} / °C	ΔH_{ss} / kJ mol^{-1}	ΔS_{ss} / J K^{-1} mol^{-1}	T_g / °C
1	63	34	100	−69	3.8	18.5	–
2	90	29	80	−12	1.3	5.0	–
3	90	39	107	–	–	–	–
4	59	27	81	–	–	–	−48
$\mathbf{1}_{0.5}\mathbf{4}_{0.5}$	40	30	97	–	–	–	–

Mechanical properties

To investigate the mechanical properties associated with the weak metal–linker interaction, thermal expansivity was calculated from VT-PXRD patterns (Fig. S15–S17, Table S4–S6). Fig. 3a–c display the relative lattice constants of **1**–**3** as functions of temperature. For **1** and **2**, temperatures above each T_{ss} were taken into account. The coefficient of thermal expansion (CTE) was -69×10^{-6} and $+370 \times 10^{-6}$ K^{-1} for the *a*/*b*- and *c*-axes of **1**, and $+69 \times 10^{-6}$, $+76 \times 10^{-6}$ and $+200 \times 10^{-6}$ K^{-1} for the *a*-, *b*-, and *c*-axes of **2**. The CTE is substantial compared to reported CP/MOFs, and is comparable to organic polymers.[31] The negative thermal expansion (NTE) in **1** is understood as a result of expansion along the *c*-axis and flexible deformation of the 3D network. As for **3**, CTE was +270, +180, and -110×10^{-6} K^{-1} for the *a*-, *b*-, and *c*-axes, across the temperature range of −100–80 °C. Both positive and negative thermal expansions are considered 'colossal', reaching the CTE as large as $\pm 100 \times 10^{-6}$ K^{-1}, and significant anisotropic expansion was observed.[32,33] NTE in **3** indicates the contraction of the Li–GN–Li linkage, suggesting the higher deformability of the longer aliphatic chain contributing to the softer mechanical property.

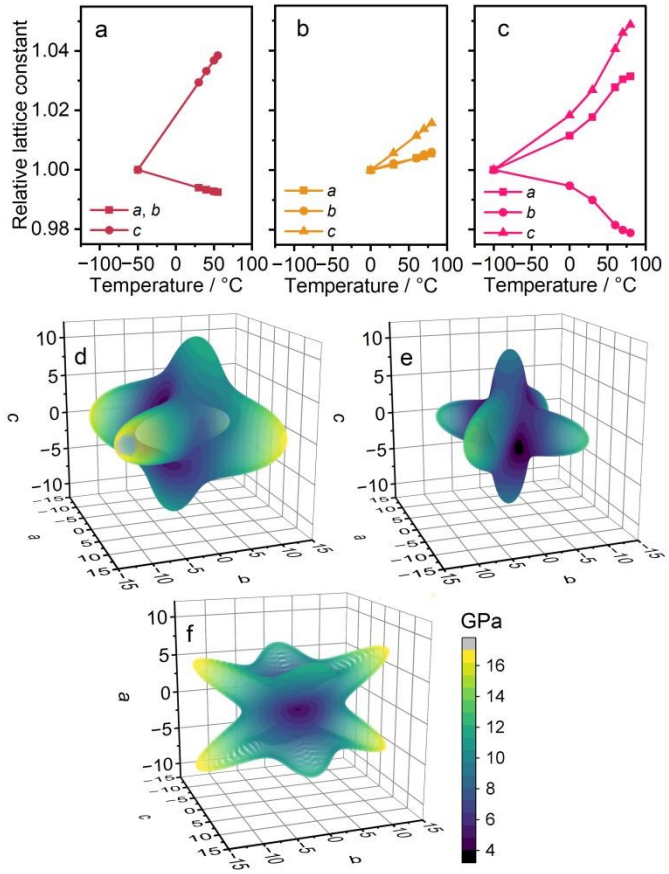

Fig. 3 Mechanical properties of **1**–**3**. Relative lattice constant of (a) **1**, (b) **2**, and (c) **3**. Computed spatial dependence of Young's moduli of (d) **1**, (e) **2**, and (f) **3**.

The mechanical properties of **1**–**3** were computed. The elastic tensors are calculated using the DFT method (Fig. S18, S19).[34,35] Fig. 3d–f show the spatial dependence of Young's moduli. The anisotropies in the *ab* plane of **1** and **2** are attributed to the low-symmetric initial structures considered in DFT calculations.[33,34] The calculated Young's moduli range 4.3–17.7 (**1**), 3.3–13.7 (**2**), and 0.3–16.8 GPa (**3**). These values are smaller compared with reported CP/MOFs, such as $Zr_6(OH)_4O_4$(1,4-benzenedicarboxylate)$_6$ (UiO-66, 37.1–46.3 GPa) or Zn_3O(1,4-benzenedicarboxylate)$_2$, (MOF-5, 9.5–19.7 GPa), suggesting the effect of the weak metal–linker interaction to the stiffness.[35,36] **1** and **2** are stiff along the Li–SN/GN–Li linkage. The smaller Young's modulus of **2** than **1** suggests the softness of the longer aliphatic chain of GN than SN. Despite the similarities in the crystal structures, **3** exhibited a different shape of spatial dependence. The low Young's modulus along the *a*-axis of **3** indicates the deformability of the zig-zag structure in the Li–SN–Li linkage.

Diffusion behaviours

Impedance measurements were conducted for **1**–**4** (Fig. S20, S21). A high transference number (0.95) and a hopping conduction mechanism of Li^+ were reported for **1**, suggesting potential opportunities for Li^+-conductivity in **2**–**4** as well.[10,37] Temperature-step DSC was conducted for **4** with the same temperature program as impedance measurement (Fig. S22), observing crystallisation at 50 °C. Ion conductivity was calculated from the semi-circles of the obtained Nyquist plot. Fig. 4 shows Arrhenius plots for the first and after-melting cycles. The conductivity (σ) of **1**–**4** at 30 °C in the after-melting cycle was 1.3, 1.5, 1.3, and 1.2×10^{-5} S cm^{-1}, and the activation energies (E_a) were 16, 13, 21, and 8 kJ mol^{-1} (Fig. S23). The comparable σ and E_a of **1**–**3** suggest the identical Li^+ hopping mechanism in the conduction. The E_a of **4** is lower by 0.5 times, suggesting different Li^+ conduction paths in **4**. The crystal of **4** is in a lower symmetry with a higher number of neighbouring Li^+ sites, and this leads to the formation of several possible Li^+ ion paths, reducing the E_a in Li^+ conduction (Fig. 4d, f). ^{7}Li T_1 relaxation time in VT solid-state nuclear magnetic resonance (SS-NMR) corroborates the E_a of conductivity. In Fig. S24, the ^{7}Li T_1 relaxation time is plotted as a function of temperature. The E_a of each ^{7}Li T_1 relaxation time followed the same trend as those of Li^+ conductivity (Table S7). This suggests the Li^+-conduction mechanism based on Li^+ hopping and the difference of E_a between **1**–**3** and **4** supports the identical Li^+ hopping mechanism in **1**–**3** and multiple conduction paths in **4**.

DOI: 10.1039/D5SC06222E

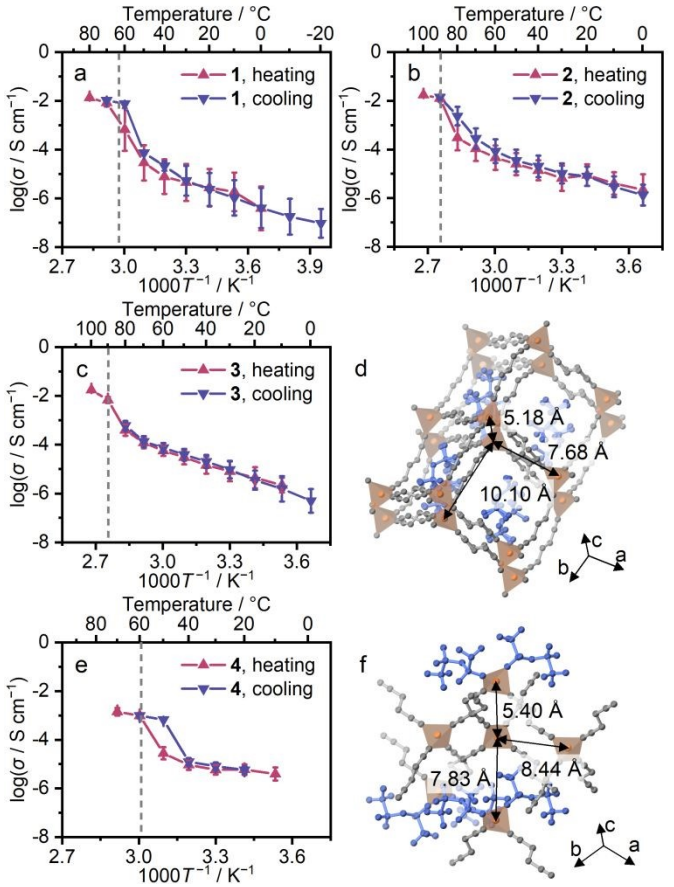

Fig. 4 Li^+ conductivity (σ) of **1**–**4**. Arrhenius plots of Li^+ conductivity of (a) **1**, (b) **2**, (c) **3**, and (e) **4**. Red and blue plots represent heating and cooling processes. The dashed lines indicate the T_m. The crystal structures of (d) **3** and (f) **4**. The distances between neighbouring Li^+ are indicated.

Conclusions

Four framework crystals, $Li(FSI)(SN)_2$, $Li(FSI)(GN)_2$, Li(FSI)(SN)(GN), and $Li(TFSI)(SN)_{1.5}$ were synthesised from Li^+ and aliphatic dinitrile linkers by a solvent-free melt-cooling process. These are constructed through weak metal–ligand interaction explained by HSAB theory, leading to low T_m below 90 °C. DFT-based elasticity analyses revealed high and anisotropic deformability, attributed to the aliphatic softness and framework topology. XRD-based thermal expansion analyses observed a large linear CTE of $+370 \times 10^{-6}$ K^{-1} in a framework, as well as a large negative thermal expansion with the CTE of -110×10^{-6} K^{-1} in another one, attributed to the structural anisotropy. AC impedance and solid-state NMR elucidated the ionic conductivity of 1.5×10^{-5} S cm^{-1} at room temperature based on the weak metal–linker interactions. This work provides clear evidence and guidelines for synthesising mechanically soft, thermally active molecular frameworks based on weak metal–linker interactions.

Author contributions

T.N. and K.K. contributed equally to this work. T.N., K.K., and S.H. conceptualised the project. K.K., T.N., T.K., N.S., S.To., S.Ts, and N.M. contributed to data collection and formal analyses. T.N. and S.H. summarised the findings in the manuscript, and all the authors approved the final version.

Conflicts of interest

There are no conflicts to declare.

Data availability

The data supporting this article have been included in the ESI. Crystallographic data for $Li(FSI)(GN)_2$, Li(FSI)(SN)(GN), and $Li(TFSI)(bpe)_2$ have been deposited at the CCDC under 2463044, 2463045, and 2480466, and can be obtained from https://www.ccdc.cam.ac.uk/structures/.

Acknowledgements

This work was supported by the Japan Society of the Promotion of Science (JSPS) for a Transformative Research Areas (A) "Supraceramics" (JP22H05147), Fund for the Promotion of Joint International Research (International Collaborative Research, JP24K0112), the Japan Science and Technology Agency (JST) for a NEXUS (JPMJNX25B4), The Asahi Glass Foundation. T.N. acknowledges SPRING (JPMJSP2110) from JST, and Ginpu Fund from the Graduate School of Science, Kyoto University. We acknowledge SPring-8 beamtime at BL02B2 and BL04B2 for PXRD (proposal nos. 2023A1748, 2023B1639, 2023B1721, and 2025B1683) with the approval of Japan Synchrotron Radiation Research Institute (JASRI). We acknowledge Drs. Takuji Hatakeyama and Masahiro Hayakawa for the opportunities for SC-XRD measurements. K.K. and T.N. thank Drs. Kazuyoshi Kanamori and Kei Morisato for the insightful discussion.

Notes and references

1 H. Furukawa, K. E. Cordova, M. O'Keeffe and O. M. Yaghi, *Science*, 2013, **341**, 1230444.
2 S. Horike, S. S. Nagarkar, T. Ogawa and S. Kitagawa, *Angew. Chem. Int. Ed.*, 2020, **59**, 6652–6664.
3 T. D. Bennett, A. K. Cheetham, A. H. Fuchs and F.-X. Coudert, *Nat. Chem.*, 2016, **9**, 11–16.
4 T. D. Bennett and S. Horike, *Nat. Rev. Mater.*, 2018, **3**, 431–440.
5 N. Ma and S. Horike, *Chem. Rev.*, 2022, **122**, 4163–4203.
6 L. León-Alcaide, R. S. Christensen, D. A. Keen, J. L. Jordá, I. Brotons-Alcázar, A. Forment-Aliaga and G. Mínguez Espallargas, *J. Am. Chem. Soc.*, 2023, **145**, 11258–11264.
7 N. Ma, S. Kosasang, E. K. Berdichevsky, T. Nishiguchi and S. Horike, *Chem. Sci.*, 2024, **15**, 7474–7501.
8 M. Liu, R. D. McGillicuddy, H. Vuong, S. Tao, A. H. Slavney, M. I. Gonzalez, S. J. L. Billinge and J. A. Mason, *J. Am. Chem. Soc.*, 2021, **143**, 2801–2811.
9 Y. Ohara, T. Nishiguchi, S. Horike and D. M. Packwood, *Inorg. Chem.*, 2025, **64**, 5682–5687.
10 K. Tanaka, Y. Tago, M. Kondo, Y. Watanabe, K. Nishio, T. Hitosugi and M. Moriya, *Nano Lett.*, 2020, **20**, 8200–8204.

11 P. Prakash, B. Fall, J. Aguirre, L. A. Sonnenberg, P. R. Chinnam, S. Chereddy, D. A. Dikin, A. Venkatnathan, S. L. Wunder and M. J. Zdilla, *Nat. Mater.*, 2023, **22**, 627–635.
12 J. Luo, Y. Chang, J.-W. Shi, X. Wang, H. Huang, Y. Zhang, X. Wang, J. Zhang, Y.-X. Huang and R. Zhao, *Nano Lett.*, 2024, **24**, 15035–15042.
13 C. Luo, C. Ning, X. Huang, P. Zhang, L. Yang, S. Wang, J. Wang, Y. Wang, K. Wan, Z.-H. Guo, K. Yue and Z. Liang, *Angew. Chem. Int. Ed*, 2025, e202507051.
14 Y. Ugata, M. L. Thomas, T. Mandai, K. Ueno, K. Dokko and M. Watanabe, *Phys. Chem. Chem. Phys.*, 2019, **21**, 9759–9768.
15 Y. Ugata, R. Tatara, K. Ueno, K. Dokko and M. Watanabe, *J. Chem. Phys.*, 2020, **152**, 104502.
16 H. Katsuragawa, S. Mori, Y. Tago, S. Maeda, S. Matsuda, H. Toriu, R. Nakayama, S. Kobayashi, T. Hitosugi and M. Moriya, *ACS Appl. Energy Mater.*, 2025, **8**, 3599–3605.
17 V. A. Blatov, A. P. Shevchenko and D. M. Proserpio, *Cryst. Growth Des.*, 2014, **14**, 3576–3586.
18 X. Zheng, K. Fukuhara, Y. Hijikata, J. Pirillo, H. Sato, K. Takahashi, S.-I. Noro and T. Nakamura, *Commun. Chem.*, 2020, **3**, 1–7.
19 X. Zheng, M. Kato, Y. Uemura, D. Matsumura, I. Yagi, K. Takahashi, S.-I. Noro and T. Nakamura, *Inorg. Chem.*, 2023, **62**, 1257–1263.
20 Y. Ohara, T. Nishiguchi, X. Zheng, S.-I. Noro, D. M. Packwood and S. Horike, *Chem. Commun.* , 2024, **60**, 9833–9836.
21 T. Nishiguchi, Y. Ohara, K. Kadota, X. Zheng, S.-I. Noro and S. Horike, *Chem. Sci.*, 2025, **16**, 621–626.
22 A. Nazet, S. Sokolov, T. Sonnleitner, T. Makino, M. Kanakubo and R. Buchner, *J. Chem. Eng. Data*, 2015, **60**, 2400–2411.
23 L. Schkeryantz, P. Nguyen, W. D. McCulloch, C. E. Moore, K. C. Lau and Y. Wu, *Inorg. Chem.*, 2021, **60**, 14679–14686.
24 T. Endo, K. Sunada, H. Sumida and Y. Kimura, *Chem. Sci.*, 2022, **13**, 7560–7565.
25 A. Wehrl, *Rev. Mod. Phys.*, 1978, **50**, 221–260.
26 A. Lang, C. Chen, C. Ye, L. N. McHugh, X. W. Chua, S. D. Stranks, S. E. Dutton and T. D. Bennett, *J. Am. Chem. Soc.*, 2024, **146**, 33945–33955.
27 K. Atthawilai, H. Tabe, K. Ohara, K. Kongpatpanich and S. Horike, *J. Am. Chem. Soc.*, 2025, **147**, 5140–5148.
28 S. Li, S. Yu, S. M. Collins, D. N. Johnstone, C. W. Ashling, A. F. Sapnik, P. A. Chater, D. S. Keeble, L. N. McHugh, P. A. Midgley, D. A. Keen and T. D. Bennett, *Chem. Sci.*, 2020, **11**, 9910–9918.
29 A. L. Goodwin, M. Calleja, M. J. Conterio, M. T. Dove, J. S. O. Evans, D. A. Keen, L. Peters and M. G. Tucker, *Science*, 2008, **319**, 794–797.
30 W. Cai and A. Katrusiak, *Nat. Commun.*, 2014, **5**, 1–8.
31 R. Golesorkhtabar, P. Pavone, J. Spitaler, P. Puschnig and C. Draxl, *Comput. Phys. Commun.*, 2013, **184**, 1861–1873.
32 R. Gaillac, P. Pullumbi and F.-X. Coudert, *J. Phys. Condens. Matter*, 2016, **28**, 275201.
33 A. U. Ortiz, A. Boutin, A. H. Fuchs and F.-X. Coudert, *Phys. Rev. Lett.*, 2012, **109**, 195502.
34 E. Kiely, R. Zwane, R. Fox, A. Reilly and S. Guerin, *CrystEngComm*, 2021, **23**, 5697–5710.
35 D. F. Bahr and J. A. Reid, *Phys. Rev. B.*, 2007, **76**, 184106.
36 H. Wu, T. Yildirim and W. Zhou, *J. Phys. Chem. Lett.*, 2013, **4**, 925–930.
37 R. Sasaki, M. Moriya, Y. Watanabe, K. Nishio, T. Hitosugi and Y. Tateyama, *J. Mater. Chem. A*, 2021, **9**, 14897–14903.

View Article Online
DOI: 10.1039/D5SC06222E

View Article Online
DOI: 10.1039/D5SC06222E

Data availability statement for

Soft crystalline properties of 2D frameworks constructed from mismatched metal and ligand pairs

Taichi Nishiguchi,‡[a] Kotoha Kageyama,‡[b] Takuya Kurihara,[c] Nanae Shimanaka,[d] Shun Tokuda,[b,d] Shuto Tsuda,[a] Nattapol Ma[b] and Satoshi Horike*[a,d,e]

[a] Department of Chemistry, Graduate School of Science, Kyoto University, Kitashirakawa-Oiwakecho, Sakyo-ku, Kyoto 606-8502, Japan
[b] Department of Synthetic Chemistry and Biological Chemistry, Graduate School of Engineering, Kyoto University, Katsura, Nishikyo-ku, Kyoto 615-8510, Japan
[c] Division of Material Chemistry, Graduate School of Natural Science and Technology, Kanazawa University, Kakuma-Machi, Kanazawa, Ishikawa 920-1192, Japan
[d] Institute for Integrated Cell-Material Sciences, Institute for Advanced Study, Kyoto University, Yoshida-Honmachi, Sakyo-ku, Kyoto 606-8501, Japan
[e] Department of Materials Science and Engineering, School of Molecular Science and Engineering, Vidyasirimedhi Institute of Science and Technology, Rayong, 21210, Thailand

‡These authors contributed equally.

*e-mail: horike.satoshi.3r@kyoto-u.ac.jp

The data supporting this article have been included in the ESI. Crystallographic data for Li(FSI)$(GN)_2$, Li(FSI)(SN)(GN), and Li(TFSI)$(bpe)_2$ have been deposited at the CCDC under 2463044, 2463045, and 2480466, and can be obtained from https:// www.ccdc.cam.ac.uk/structures/.